

See discussions, stats, and author profiles for this publication at: <https://www.researchgate.net/publication/308342142>

# In Situ Atomic Level Dynamics of Heterogeneous Nucleation and Growth of Graphene from Inorganic Nanoparticle Seeds

Article in ACS Nano · September 2016

DOI: 10.1021/acsnano.6b04356

CITATIONS

6

READS

117

8 authors, including:



**Chuncheng Gong**  
University of Oxford

15 PUBLICATIONS 371 CITATIONS

[SEE PROFILE](#)



**Kuang He**  
University of Oxford

39 PUBLICATIONS 2,520 CITATIONS

[SEE PROFILE](#)



**Gun-Do Lee**  
Seoul National University

105 PUBLICATIONS 2,410 CITATIONS

[SEE PROFILE](#)



**Qu Chen**  
University of Oxford

16 PUBLICATIONS 659 CITATIONS

[SEE PROFILE](#)

Some of the authors of this publication are also working on these related projects:



Van der waals heterojunctions [View project](#)



Low Energy Systems Technology (LEAST) [View project](#)

# In Situ Atomic Level Dynamics of Heterogeneous Nucleation and Growth of Graphene from Inorganic Nanoparticle Seeds

Chuncheng Gong,<sup>†,||</sup> Kuang He,<sup>†,||</sup> Gun-Do Lee,<sup>\*,‡</sup> Qu Chen,<sup>†</sup> Alex W. Robertson,<sup>†</sup> Euijoon Yoon,<sup>‡</sup> Suklyun Hong,<sup>§</sup> and Jamie H. Warner<sup>\*,†</sup>

<sup>†</sup>Department of Materials, University of Oxford, Parks Road, Oxford OX1 3PH, United Kingdom

<sup>‡</sup>Department of Materials Science and Engineering, Seoul National University, Seoul 151-742, Korea

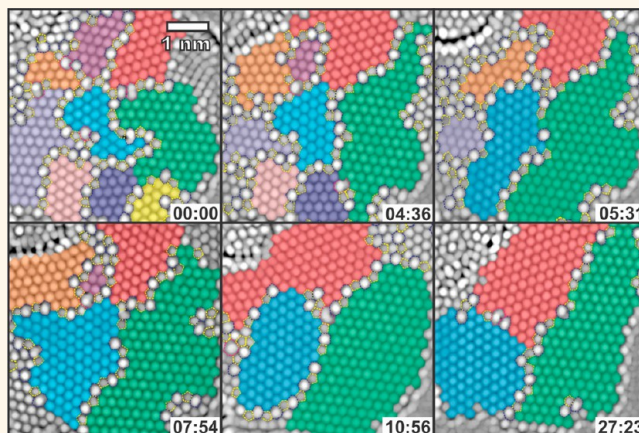
<sup>§</sup>Department of Physics and Graphene Research Institute, Sejong University, Seoul 143-747, Korea

## S Supporting Information

**ABSTRACT:** An *in situ* heating holder inside an aberration-corrected transmission electron microscope (AC-TEM) is used to investigate the real-time atomic level dynamics associated with heterogeneous nucleation and growth of graphene from Au nanoparticle seeds. Heating monolayer graphene to an elevated temperature of 800 °C removes the majority of amorphous carbon adsorbates and leaves a clean surface. The aggregation of Au impurity atoms into nanoparticle clusters that are bound to the surface of monolayer graphene causes nucleation of secondary graphene layers from carbon feedstock present within the microscope chamber. This enables the *in situ* study of heterogeneous nucleation and growth of graphene at the atomic level. We show that the growth mechanism consists of alternating C cluster attachment and indentation filling to maintain a uniform growth front of lowest energy.

Back-folding of the graphene growth front is observed, followed by a process that involves flipping back and attaching to the surrounding region. We show how the highly polycrystalline graphene seed evolves with time into a higher order crystalline structure using a combination of AC-TEM and tight-binding molecular dynamics (TBMD) simulations. This helps understand the detailed lowest-energy step-by-step pathways associated with grain boundaries (GB) migration and crystallization processes. We find the motion of the GB is discontinuous and mediated by both bond rotation and atom evaporation, supported by density functional theory calculations and TBMD. These results provide insights into the formation of crystalline seed domains that are generated during bottom-up graphene synthesis.

**KEYWORDS:** AC-TEM, graphene, GB, *in situ* TEM, crystallization, grain growth



Chemical vapor deposition (CVD) of graphene on Cu substrates has been a promising method to synthesize large-area graphene with industrial scalability.<sup>1–6</sup> Graphene domains nucleate on the Cu surface and grow larger as precursor feedstock is supplied until they eventually merge together to form a continuous polycrystalline film.<sup>7</sup> The formation of graphene domains can be either from heterogeneous and homogeneous nucleation processes. Heterogeneous nucleation involves using seeds, often particles, to lower the precursor concentration threshold for nucleation to occur compared to homogeneous nucleation.<sup>8,9</sup> Understanding these initial nucleation processes of graphene domains is critical for developing new synthetic strategies for CVD growth of high-quality graphene continuous films. Previous results have shown

that individual graphene domains can be single crystals, but in some cases are polycrystalline.<sup>1,8,10–12</sup> Having polycrystallinity from a single domain region significantly increases the number of grain boundaries (GB) in the final continuous films of graphene as the domains merge together.

The GBs can impact the mechanical,<sup>13–18</sup> electrical,<sup>8,19,20</sup> and chemical properties of graphene.<sup>21</sup> The atomic structure of dislocations and GBs in graphene has been investigated in both experimental and theoretical calculations, primarily for the

Received: July 1, 2016

Accepted: September 12, 2016

Published: September 19, 2016

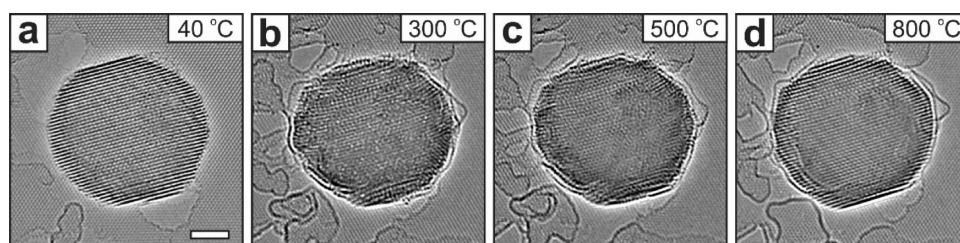


**Figure 1.** AC-TEM images of a Au nanoparticle sitting on a multilayer graphene sheet in the temperature range between 40 and 800 °C. The scale bar in panel a is 3 nm.

potential application in device fabrication and nanoengineering.<sup>22–32</sup> In 1988, Albrecht *et al.* reported the observation of tilted GBs in graphite using scanning tunneling microscopy (STM).<sup>33</sup> It was not until many years later that the atomic structure comprised of arrangements of pentagon–heptagon (5–7) edge dislocations was revealed by high-resolution transmission electron microscopy (TEM) experiments.<sup>34</sup> Similar results were later achieved by multiple TEM and STM observations.<sup>35–37</sup> The formation of 5–8–5 linear GBs has also been reported in polycrystalline graphene grown on Ni (111) substrate due to the strong graphene–substrate interaction.<sup>38</sup> Experimental studies of the atomic level migration of a GB using an aberration-corrected TEM (AC-TEM) revealed migration mediated by bond rotations, however *ab initio* theoretical calculations indicate that GBs can also migrate by evaporation of a carbon dimer.<sup>36,39</sup> After high-temperature annealing (600 °C), curved and aperiodic GBs in CVD grown graphene reconstruct into straighter and periodic forms.<sup>37</sup> *In situ* experiments within a TEM at high temperatures of 2000 K by Joule heating found carbon adsorbates on monolayer graphene transformed into polycrystalline graphene domains separated by GBs.<sup>40</sup> Reconfiguration of carbon bonds at the GBs was found to give rise to better crystallinity.

Prior work using AC-TEM to study *in situ* growth of graphene has shown that carbon can attach to pre-existing edges of graphene to further continue its growth. Liu *et al.* reported the *in situ* growth of a second-layer graphene inside a AC-TEM from the step edge of an existing domain under beam irradiation.<sup>41–45</sup> The crystallinity and growth rate of the newly grown area were shown to be temperature dependent, with single silicon atoms located at the step edge suggested to act as a catalyst for second-layer graphene growth from hydrocarbons.<sup>36</sup> Homogenous nucleation of small graphene seeds is often studied by STM and can reveal the transition from a molecular disordered cluster to small crystalline fragments of sp<sup>2</sup> carbon.<sup>46</sup> However, there are hardly any atomic level studies related to heterogeneous nucleation of graphene domains from seeds, such as metal nanoparticles.

In this report, we utilize an *in situ* heating holder within an AC-TEM to study the heterogeneous nucleation and growth of graphene from metal nanoparticles seeds. We also study the growth of the graphene domain size in regards to the site-specific addition of carbon atoms and also the GB transformations that underpin the increase in crystallinity of the domains. The initial graphene was synthesized by ambient pressure CVD method using melted copper on molybdenum substrate as the catalyst as previously reported.<sup>10,47</sup> The graphene sheet was subsequently transferred onto a SiN grid designed for *in situ* high-temperature TEM experiments (DENSolutions). The heating holder allows us to accurately

control the specimen temperature from room temperature to 800 °C and capture detailed real-time dynamics.

## RESULTS AND DISCUSSION

Monolayer graphene was first heated up to 800 °C inside the TEM using the *in situ* heating holder (Figure 1a), which causes the amorphous carbon surface adsorbates to evaporate and reveal the lattice structure of graphene. This effect has also been

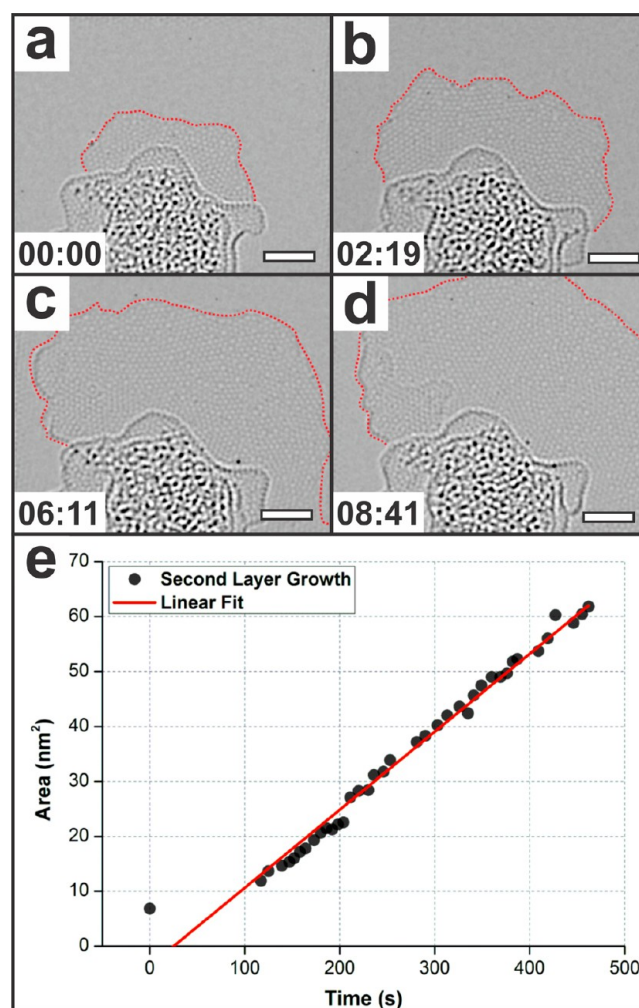


**Figure 2.** (a–d) Time series of AC-TEM images showing the growth of a secondary graphene layer from surface adsorbate attachment. The frontier for the second layer is shown by the red dotted lines. The underlying monolayer graphene has been removed from the images using a filter mask in the Fourier transform. All scale bars = 3 nm. (e) The area for the as-grown second layer is plotted against time.

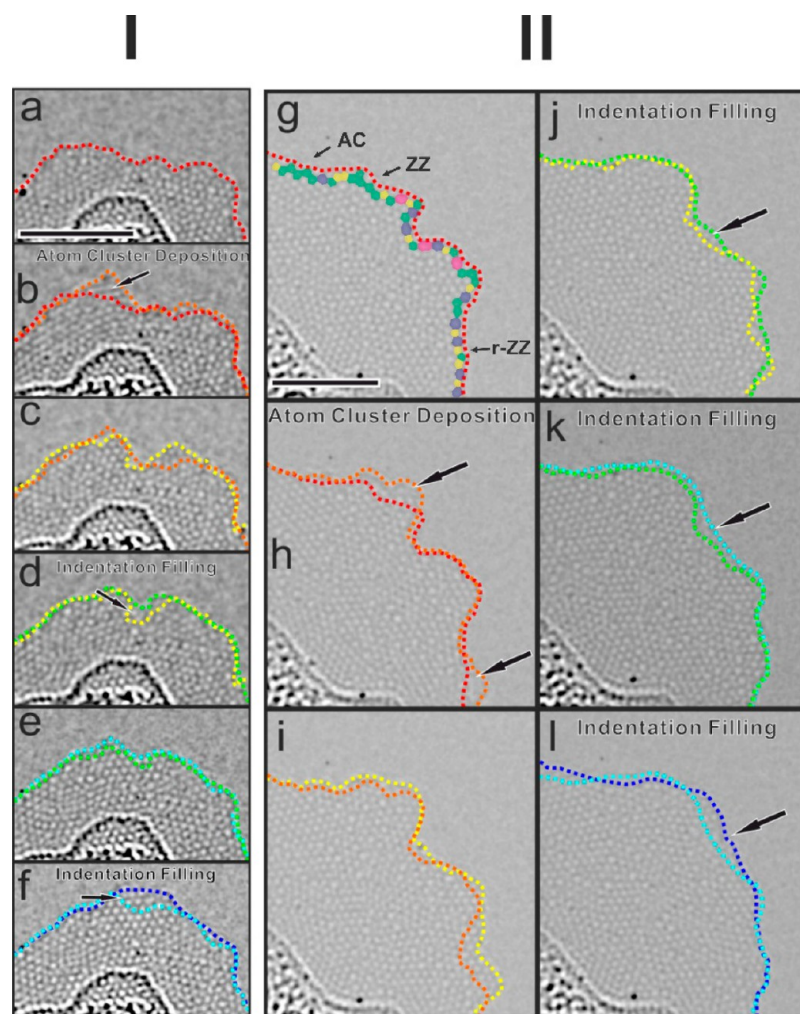


**Figure 3.** Two different examples, (a–f) and (g–l), showing *in situ* atomic level dynamics of the graphene edge growth. The time series of AC-TEM images show the cluster addition of C atoms to the edges of amorphous graphene domains. Time between frames is  $\sim 10$  s. The perimeters are color coded differently to allow visual comparison between the two consecutive frames. The color scheme in panel g represents the number of carbon atoms in each ring at the edge, with 5 = yellow, 6 = green, 7 = blue, and 8 = pink. All scale bars = 3 nm. The underlying monolayer graphene has been removed by a filter mask in the Fourier transform.

described with more detail in previous experiments.<sup>48,49</sup> However, an increase in the specimen temperature causes the metal nanoparticles to be encapsulated with carbon “graphitic” shells.<sup>50</sup> Figure 1a shows a nanoparticle with radius of  $\sim 10$  nm at room temperature supported on a multilayer graphene sheet. Energy-dispersive X-ray spectroscopy (EDX) taken on the nanoparticle shows they are Au (see Figure S2 for further details). The Si atoms from contamination during the CVD growth and transfer process may also be present in the nanoparticle. When we increase the temperature up to 300 °C, the nanoparticles start to get encapsulated by few-layered graphene fragments as shown in Figure 1b. No apparent change happens to the core–shell structure when we further increase the specimen temperature to 500 and 800 °C (Figure 1c,d). Early research has shown that the melting point of Au nanocluster drops below 800 °C when the particle radius is  $< 3$  nm.<sup>51</sup> Accordingly, we observe the Au nanoparticle with  $\sim 5$  nm diameter in Figure 2a appears amorphous and partially evaporated when the specimen is heated to 800 °C, thus revealing the boundary of the carbon shell and the particle before melting. 600 °C was found to be the optimal temperature where hydrocarbons attach to the seed and

begin to slowly grow graphene. At 800 °C, the rate of graphene growth basically reached an equilibrium with the etching of edge atoms, and the formation of a secondary layer of graphene is limited.

According to the classical nucleation theory, heterogeneous nucleation is much more commonly observed as oppose to homogeneous nucleation, and the reaction process is also much faster due to the lower nucleation energy barrier. In the case of the *in situ* high-temperature graphene growth in the AC-TEM, electron beam irradiation of the pristine monolayer graphene area did not lead to the formation of a secondary layer of graphene on top. However, around the Au particles, a secondary layer of graphene nucleates swiftly and continues to grow at 600 °C. Figure 2a–d shows a time series of secondary layer growth with the underlying monolayer graphene removed from image using a mask filter in the Fourier transform, similar to those shown in Figures 4 and 6. The growth rate is shown in Figure 2e by plotting the area of the secondary layer with time for all 39 frames over 8 min 41 s. Excluding the odd first point, the results exhibit an excellent linear relationship. The growth rate obtained from the slope of

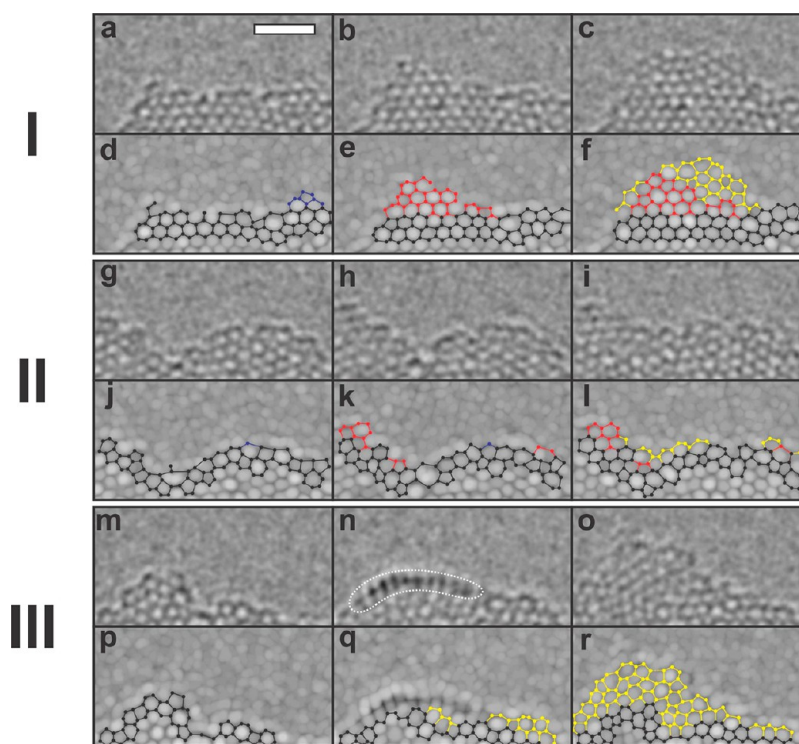


**Figure 4.** Another three sets of sequential AC-TEM images showing the edge growth and reconstruction of second-layer graphene at higher magnification: (a–c) carbon cluster deposition; (g–i) indentation filling; and (m–o) back-folding of the edge. Time between frames is  $\sim 10$  s. (d–f), (j–l), and (p–r) Corresponding maximum filtered images with original edges colored in black. Atoms attached to the edge in next frames are colored in red and yellow. Edge atoms to be etched are highlighted in blue. The scale bar in panel a is 1 nm.

the linear equation is  $0.14 \text{ nm}^2/\text{s}$ . This relatively slow growth rate enables us to study the dynamics of the growth frontier.

The growth front is carefully studied to gain a deeper understanding of how the domain gradually expands its size atom by atom. At first glance, the advance of the growth front is accomplished by alternant “carbon cluster deposition” and “indentation filling”, shown in Figure 3. For example, in Figure 3a–f, where the time series of AC-TEM images are examined, a cluster of atoms adds onto the pre-existing graphene to continue the growth process, indicated by the arrow Figure 3b. This leads to the roughening of the edge in this local region, and subsequent frames show that further atom cluster deposition fills in around this to smooth the edge back out. This process of “indentation filling” is highlighted in Figure 3d,f and a second example is presented in Figure 3g–l.

We now discuss the theory for the *in situ* growth of second-layer graphene. The dependence of growth rate on temperature, beam current density and residual hydrocarbon gas pressure has been well investigated in Liu *et al.*'s previous research. Our experiment was carried out under similar conditions (see Methods), and the growth rate ( $0.14 \text{ nm}^2/\text{s}$ ) we obtain in Figure 2 is also comparable to their results. However, apart from the zigzag (ZZ), armchair (AC), and reconstructed zigzag (r-ZZ) edges, the growth front also contains a certain amount of nonperiodic structure and even some octagons (Figure 3g), which leads to poorer crystallinity of the top graphene layer compared with the previous work. The crystallinity and atomic structure of the second layer will be discussed with more detail in Figure 7. Here, we provide two possible explanations that are (i) the carbon shells in Figure 2 and 3 acting as the initial seeds for the *in situ* growth are not well crystallized and show lots of nonhexagonal rings indicative

of amorphous 2D carbon or highly defective graphene, which could give rise to similar atomic structure in the newly grow area around it, or (ii) the hydrocarbon gas concentration near the Au nanoparticle is slightly oversaturated, resulting the increase desorption rate of carbon adatoms and the lack of time to form a periodic and low-energy edge structure. Research on CVD graphene growth has shown that the growth limiting step for the reaction is the attachment of carbon adatom species to the graphene edge, and the rate of this step can be given by

$$R \propto \exp\left(-\frac{E_b}{kT}\right)$$

where  $E_b$  is the free energy barrier,  $k$  is the Boltzmann constant, and  $T$  is the experimental temperature.<sup>7</sup> The energy barriers to attach carbon adatoms to a pristine ZZ and AC edge are 2.19 and 2.47 eV, respectively.<sup>52</sup> The stability of r-ZZ edge lies between them.<sup>53</sup> Thus, it is energetically favorable to first incorporate carbon atoms onto the ZZ and r-ZZ edge when the growth front is smooth, which matches our observation in Figure 3g,h (carbon cluster deposition).

Figure 4a–c shows examples at a higher magnification, where carbon clusters containing 32 and 39 atoms are successively attached to the ZZ edge of graphene in the next two consecutive frames. The added carbon atoms may come from the edge structure colored in blue in Figure 4a, which is subsequently etched under electron irradiation, indicating that the reconfiguration of newly attached structure also takes place during the growth process. When the curvature of the growth front exceeds a certain value, filling the indentation sites becomes preferable since the decrease in surface energy partially compensates the barrier, which is also experimentally observed in Figures 3d–f,j–l and 4g–i. This provides a

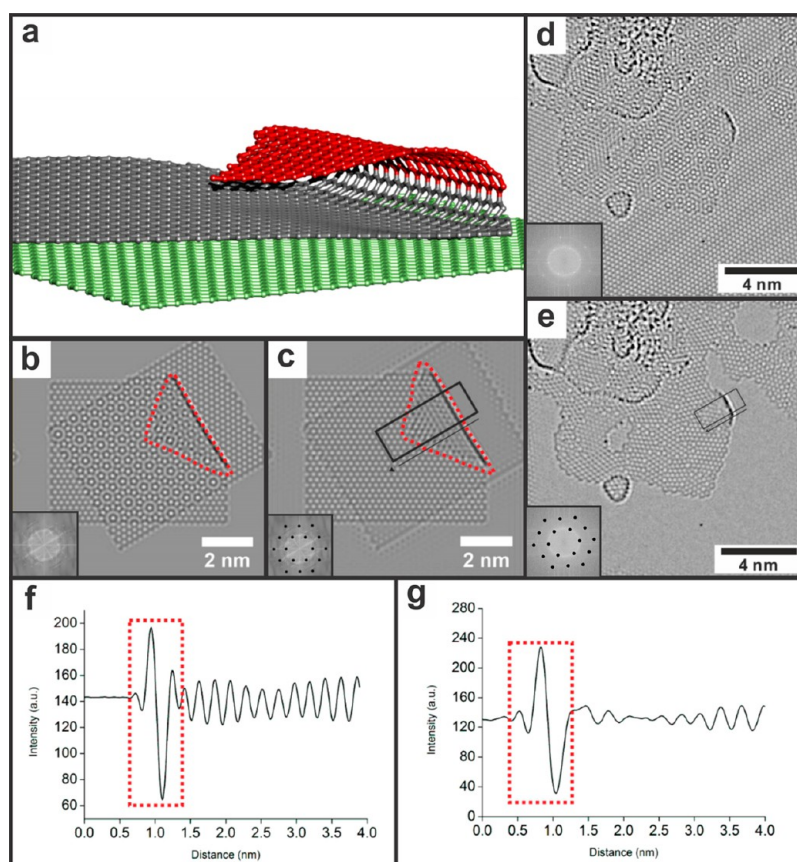


**Figure 5.** Back-folding of the secondary layer of graphene. (a) Schematic illustration of the secondary layer of graphene being folded back. (b) Multislice image simulation of the atomic model in (a) with the inset showing the FFT of the simulated image. (c) Reconstructed images from the FFT negative mask, shown in the respective inset. (d) AC-TEM image of bilayer graphene with folded edge. (e) Reconstructed image from the FFT negative mask in the respective inset. (f and h) Intensity profiles taken from the boxed regions in (c) and (e) along the directions indicated by the arrows.

theoretical basis of why the *in situ* graphene growth is an alternating process of “carbon cluster deposition” and “indentation filling”, rather than a uniform process in all directions by single atom attachment at all edge sites.

During the growth process, we repeatedly observed increased contrast at the growth front due to back-folding compared to other edge regions, as shown in Figure 4m–o with the white dashed area. We increased the temperature from 600 to 800 °C to slow down the growth rate so that we could investigate the atomic configuration of the edges and also the crystallization from amorphous to  $sp^2$ . Figure 5a is the side view of an atomic model of a back-folded secondary layer of graphene, with corresponding multislice image simulations shown in Figure 5b. A red dashed line in Figure 5b indicates the back-folded region. It is apparent that the contrast along the folding pleat increases dramatically. In order to quantify this, an image is reconstructed from the fast Fourier transform (FFT) using an exclusion mask for the set of hexagonal spots associated with the underlying graphene (inset in Figure 5c). A boxed line profile, Figure 5f, was taken from the black rectangle highlighted region along the direction shown with a black arrow in Figure 5c. Figure 5d shows an AC-TEM image of a region of secondary layer graphene, whose presence is evident from the Moiré pattern. The reconstructed image in Figure 5e excludes the signal from the bottom graphene layer, leaving only the secondary layer graphene for analysis. A boxed line profile figure is also taken from the black boxed region along the arrowed direction, and

the result is presented in Figure 5g. The red dashed box highlights the region with apparent enhanced contrast, accordant with what is observed in the multislice image simulation in Figure 5f. As have been previously reported,<sup>54,55</sup> the increase in contrast originates from multiple atoms under the projection of electron beam along the back-fold. However, it is difficult to determine whether the secondary layer of graphene is folded back or just bonded to the first graphene layer, as both introduce an increase in contrast (Figure S2).

Studying the dynamics of the back-folded region of the secondary layer of graphene provides further insights into the structure. Figure 6a–d contains a time series of AC-TEM images with red dashed lines highlighting the frontier of the secondary layer and shown in the inset. Figure 6e–h shows reconstructed images from the negative masked FFT shown in the insets. Red rectangles highlight the areas of interest, which are magnified and shown in Figure 6i–l, respectively. Figure 6i shows a dark contrast line that was previously discussed originating from back-folding or possibly bonding to the bottom layer. In this time series study, we could see the darker contrast along the edge in Figure 6j fades away in the subsequent two frames (Figure 6k,l), an area of extra graphene extends out where there used to be the darker contrasted boarder over the course of just 10 s. This indicates the extra area came from the unfolding of the folded area. The red dashed line in Figure 6k highlights the extra region formed in the unfolding process. Figure 6m–p demonstrates this process

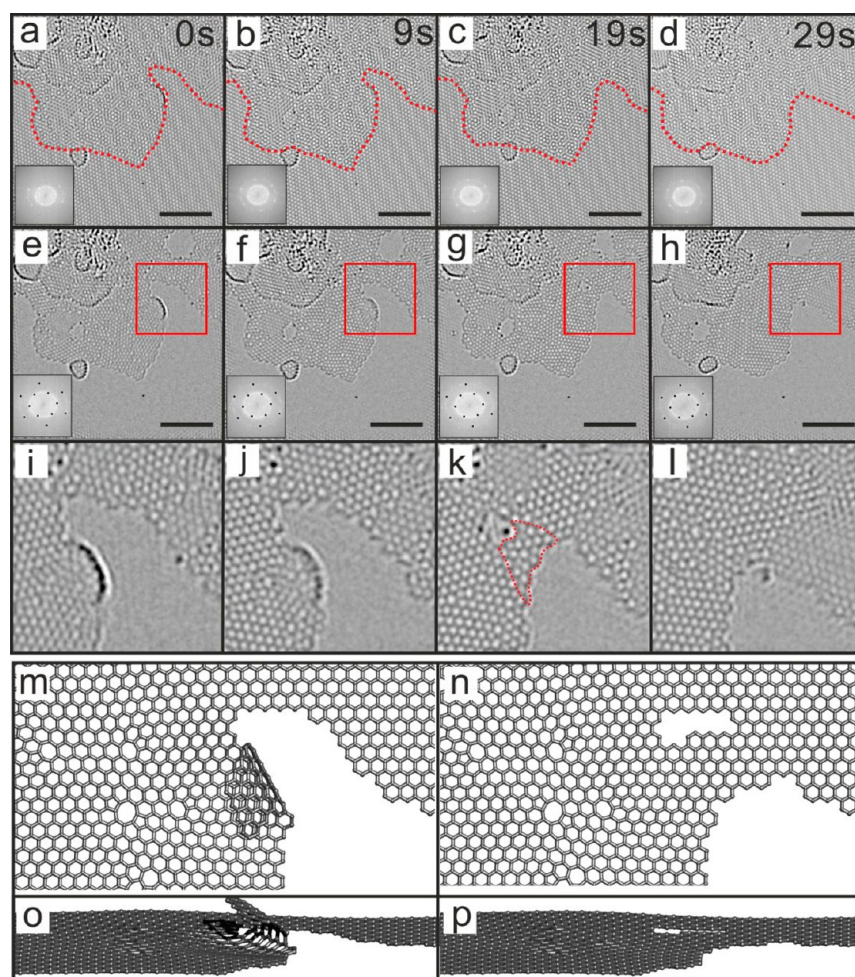


**Figure 6.** Dynamics of an unfolding graphene layer at 800 °C. (a–d) Time series of AC-TEM images showing a secondary layer of graphene initially grown at 600 °C and then examined at 800 °C. The FFTs are shown in the respective insets. (e–h) Reconstructed images from the FFT negative mask shown in the respective insets. (i–l) Magnified AC-TEM images taken from the red boxed regions in (e–h) to highlight the unfolding dynamics. (m–p) Front and side views of the atomic models before and after unfolding. All scale bars = 4 nm.

with atomistic models: with Figure 6m showing the folded model and Figure 6n showing the structure after unfolding. Figure 6o,p shows the side views of the two models, respectively. This study of the edge dynamics of the secondary layer of graphene confirms the darker contrast arises from back-folding rather than edge bonding.

Once the graphene domains reach a certain size, crystallization begins to be a dominant structural factor. The small graphene domains are initially highly polycrystalline and then begin to improve their ordering at high temperatures, achieving a better  $sp^2$  structure, and Figure 7 shows this in detail for the elevated temperature of 800 °C. Our data set in total consists of 72 AC-TEM images taken over 34 min 07 s. Figure 7a shows the same image as Figure 6a but in higher magnification in order to examine the atomic scale lattice configuration. The image is then filtered using a mask in the FFT to eliminate the underlying monolayer graphene and reconstructed (Figure 7b), then maximum filtered (Figure 7c) for better visualization of nonhexagonal rings. Yellow circles in Figure 7b highlight heavier atoms (probably Au) trapped in graphene and at the edge. In Figure 7d the crystalline area in the image is shaded with color, and the nonhexagonal rings are marked by the dashed polygons. It is apparent that a large proportion of the top layer is comprised of well-crystallized graphene grains.

However, the lattice orientation of each grain is randomly distributed, and the grain size is in the nanoscale, from 1 to 2 nm. There is also a large amount of pentagons and heptagons and several octagons at the boundary of the grains. The majority of the GBs can be regarded as highly aperiodic and curved 5–7 dislocation strings. This result is similar to the TEM images taken by Westenfelder *et al.* at 1000 K for graphene transformed from amorphous carbon.<sup>40</sup>

As reported in our previous work, both glide and climb motions for dislocation in graphene can be significantly accelerated at temperatures above 500 °C under 80 kV electron irradiation.<sup>56</sup> Therefore, as expected, we observed subsequent migration of GBs and crystallization of nanosized grains over time. Figure 7d–i shows a time series of AC-TEM images of the crystallization with the images processed the same way as Figure 7c. A dozen graphene grains have merged into 3 larger ones with sizes of 2–5 nm in the first 11 min. Sinuous GBs with high curvature tend to reconstruct into a more symmetric and straight shape over the whole time period. The growth rates for the domains shaded in green and cyan are plotted in Figure 7j as the form of the number of undistorted hexagons within the domain *versus* time. The growth process for both grains is discontinuous. Take the grain shaded in green, for example, despite the apparent shape reconfiguration

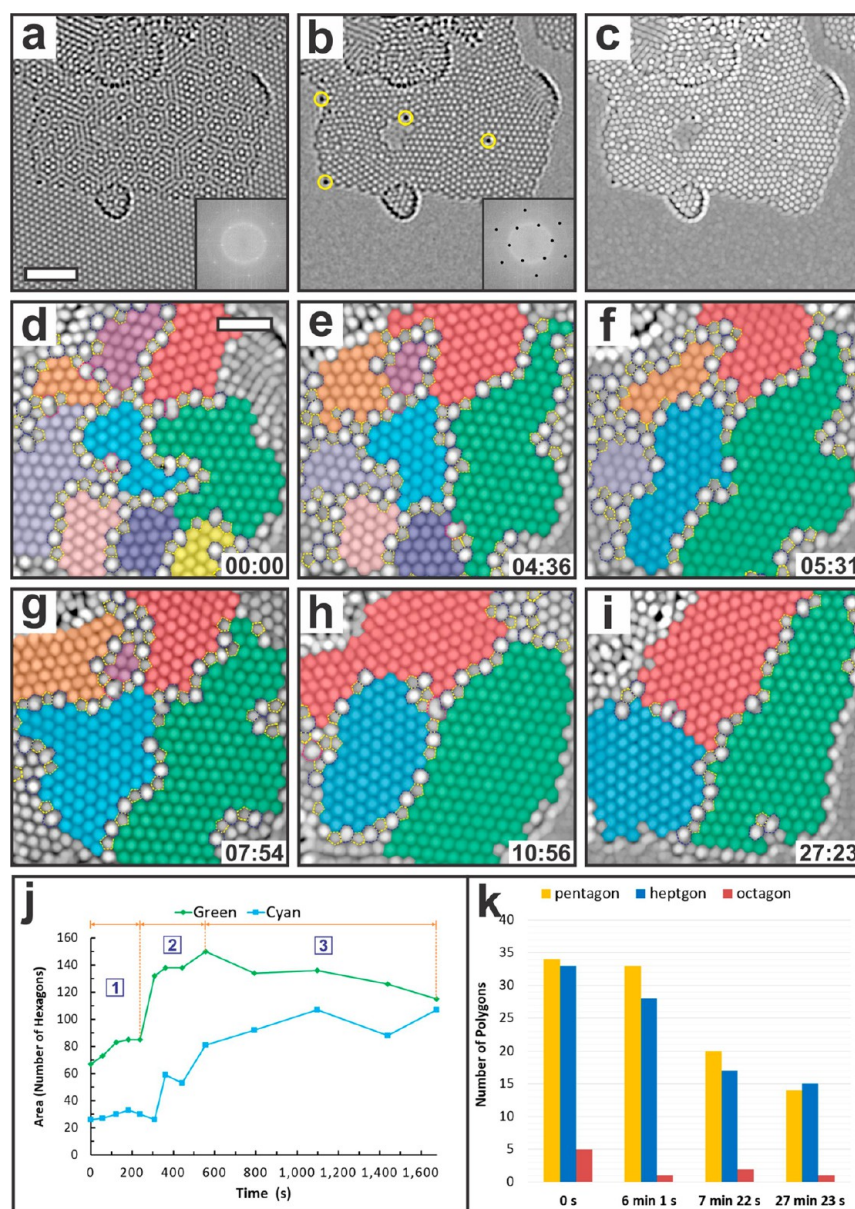


**Figure 7.** Crystallization of the as-grown graphene layer over time at 800 °C. (a–c) Image processing details: (a) Cropped from Figure 6a and then magnified with the inset showing its FFT; (b) reconstructed image from FFT negative mask shown in the inset showing the top graphene layer; and (c) maximum filtered image of (b). (d–i) Six time series frames showing the growth and coalescence of graphene grains, overlaid with false colors. The pentagon, heptagon, and octagon in the GBs are indicated by the dashed yellow, blue, and pink polygons, respectively. (j) Two trend lines representing the size change of the grains shaded in blue and cyan as a function of time. (k) Statistics of nonhexagonal rings in the GBs. Topological defects within the grain or at the edge are not included. The scale bars in panel a and d are 2 and 1 nm, respectively.

of GBs in the first 4 min (Figure 7d,e), the grain size does not change much (Stage 1, T1). A sudden change in the grain size took place between 4 and 9 min by consuming smaller grains colored in purple and yellow (Stage 2, T2). No more grain merging is observed afterward, but the movement of GBs continues at a much slower rate, leading to the gradual shrinkage of grain size in the next 19 min (Stage 3, T3). The evolution of the cyan grain is similar. The statistics in Figure 7k shows that significant reduction in nonhexagonal rings occurs between 6 min 1 s and 7 min 22 s, approximately the same period when the coalescence took place.

In Figure 8, we examine the coalescence of grains colored in cyan and pink in Figure 7e at the atomic level. The structural change between Figure 8a,b is accomplished by three sequential

SW bond rotations within 22 s, as schematically illustrated in the atomic models shown in Figure 8e–h. Insights into the sequential order are provided by high-temperature tight-binding molecular dynamics (TBMD) simulations (Supporting Information, Movie 1). We find that the bond rotations are initiated at the junction of three highly curved GBs, where there is a high density of nonhexagonal rings (Figure 8a,c,e). It has been shown that bond rotation and atom loss are more likely to occur in the defective area under electron beam irradiation due to a lower sputtering cross section.<sup>28</sup> Our recent work also shows that such a phenomenon becomes more pronounced at elevated temperatures.<sup>56</sup> In Figure 8i, we calculated the energy barriers for all three rotations using density functional theory (DFT) which are 4.57, 5.03, and 4.81 eV, respectively; all



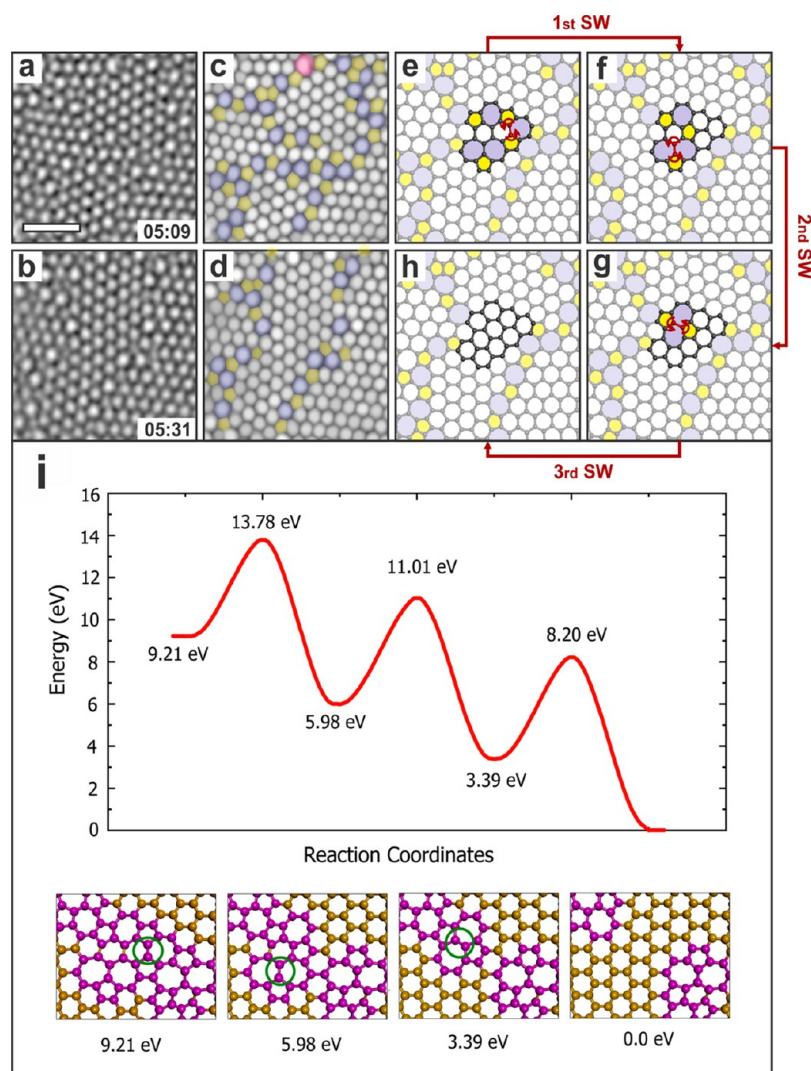
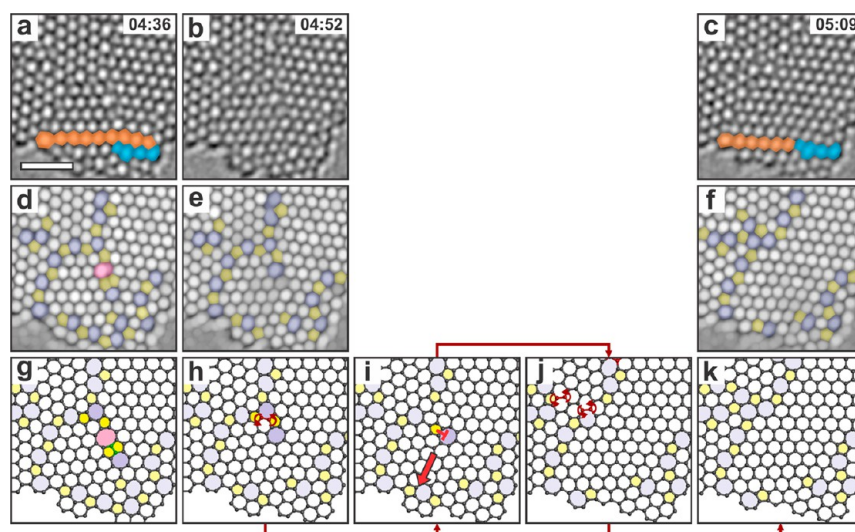


**Figure 8.** The merging of two grains *via* three bond rotations. (a,b) FFT reconstructed AC-TEM images showing the atomic structure of the second layer graphene at 5 min 9 and 22 s later. (c,d) Maximum filtered images calculated from (a,b) with nonhexagonal rings shaded in color. (e,h) Atomic models corresponding to (a) and (b). (e–h) A probable pathway for the detailed structural change between the GBs in (a) and (b) suggested by high-temperature TBMD simulations. The arrows and atoms highlighted in red indicate the bond undergoes a SW bond rotation in the next panel. The color scheme in the maximum filtered images and atomic models represents the number of carbon atoms in each ring, with 5 = yellow and 7 = blue. (i) DFT calculated energy barrier for the pathway shown in (e–h). The scale bar in panel a is 1 nm.

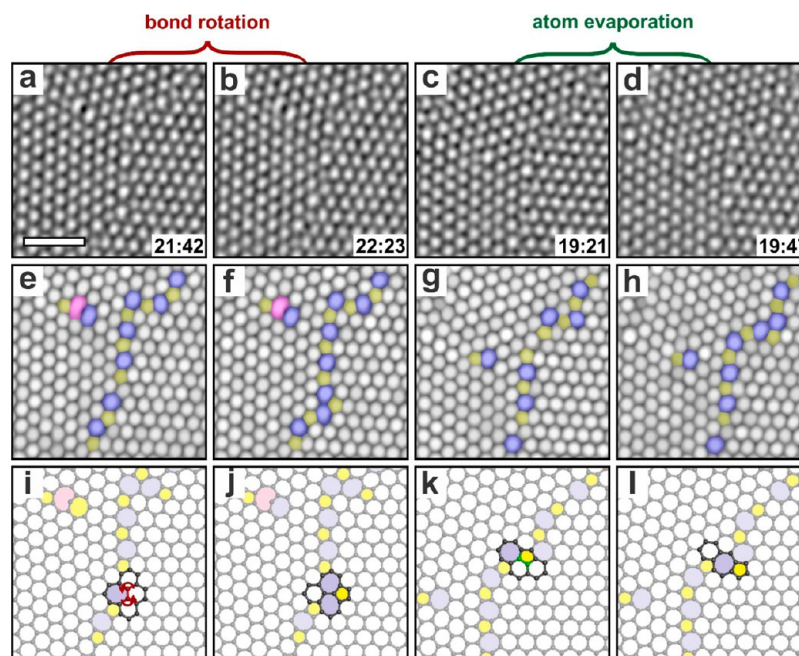
significantly lower than the energy required to form a SW defect (9–10 eV) or dislocation glide (6.95 eV).<sup>56–58</sup> The energy for each bond rotation to reverse back is more than 3 eV higher. This explains why the GBs unwound so rapidly in T2, and that the temporal resolution of our imaging was insufficient to capture any intermediate structure. As a consequence of the structural reconfiguration in Figure 8a–h, the total energy of the second layer graphene is decreased by 9.21 eV with the curvature of GBs greatly reduced, as shown in Figure 8b,d,h, which is in agreement with previous research indicating that the driving force for GB migration energetically favors decreasing GB length and curvature.<sup>36</sup> Another similar example is given in Figure S3, where 10 bonds rotate in a time span of 13 s leading to the incorporation of a small graphene grain into a larger one.

Figure 9 shows how dislocation movement can play an important role in grain merging at the edge regions. The grains to be merged are the ones shaded in blue and green in Figure 7d. A carbon dimer was removed from the GB after 16 s, resulting in the 5–8–5–5–7 defect at the boundary,

reconfiguring into a 5–7 edge dislocation and the 5° angle mismatch in Figure 9a partly compensated (Figure 9b). The GB totally annihilates after another 17 s (Figure 9c). The individual steps for this transformation were not resolvable in our imaging conditions. Figure 9h–k shows a plausible pathway by forming an isolated dislocation core at the first instance (Figure 9i). The dislocation then disappears by gliding toward the edge along its glide plane (indicated by the red arrow in Figure 9i), making the lattice mismatch eventually compensated. Recent work investigating the interactions between dislocations and graphene edges has shown it is energetically favorable for a dislocation to glide toward the edge of graphene, provided the distance is close enough.<sup>59</sup> The structural change between Figure 9j and k was accomplished by two further bond rotations. Evidence to support this is highlighted in Figure 9a,c. Two rows of zigzag-oriented graphene lattice are colored in cyan and orange in Figure 9a for visual reference. They change into one zigzag row in Figure 9c, which can only result from the slip behavior of an edge dislocation.



**Figure 9.** The coalescence of two grains *via* the slip of an edge dislocation toward the edge. (a) FFT reconstructed image of the second-layer graphene at 4 min 36 s, which loses a carbon dimer at GB in the next frame, shown in (b). (c) A following image showing annihilation of GB and merging of two grains at graphene edge. (d–f) Maximum filtered images of (a–c). (g–k) Atomic models of (a–c). (h–k) A possible path for the structural reconfiguration between panels b and c. A SW rotation first transforms the GB into an isolated pentagon–heptagon configured dislocation (i), which subsequently disappears by gliding to the edge. Bonds that undergo a SW rotation in the next frame are highlighted in red and by arrows. Atoms to be sputtered are highlighted in green. The color scheme in the maximum filtered images and atomic models represents the number of carbon atoms in each ring, with 5 = yellow, 7 = blue, and 8 = pink. The scale bar in panel a is 1 nm.



**Figure 10.** Bond rotation and dimer evaporation within the GB. (a,b) AC-TEM images showing a single bond rotation. (c,d) AC-TEM images of GB migration by sputtering a carbon dimer. (e–h) Maximum filtered images. (i–l) Atomic models. The scale bar in panel a is 1 nm.

After the first 11 min, the original nanosized grains merged to form three larger ones (colored in cyan, red, and green in Figure 7h). Instead of combining into an even larger grain, only occasional bond rotation and atom loss occurred in or near the GBs over the next 17 min (Figure 10), similar to the basic glide and climb step of a 5–7 dislocation core.<sup>27</sup> The relatively slow migration rate enables us to trace the structural change of the second layer atom by atom between each frame. In Figure 11, we observed the intermediate structure before a carbon dimer was completely sputtered from GB. The defect structure in Figure 11a remained stable for 35 s, before a carbon atom

acquired enough energy in an electron collision to break two  $sp^2$  bonds and rotate perpendicular to the graphene plane (Figure 11b). The magnified view and its corresponding multislice simulated TEM image on top of Figure 11b show that the vertically stacked carbon dimer has a higher intensity than other carbon atoms. The dimer was at last removed out of the graphene plane in another 32 s. In Figure 12, we compare the energy barriers of two mechanisms to evaporate a carbon dimer. The flipping of the dimer first needs to overcome a barrier of 9.26 eV. The vertically stacked structure is surprising stable with the energy only 2.41 eV higher than ground state

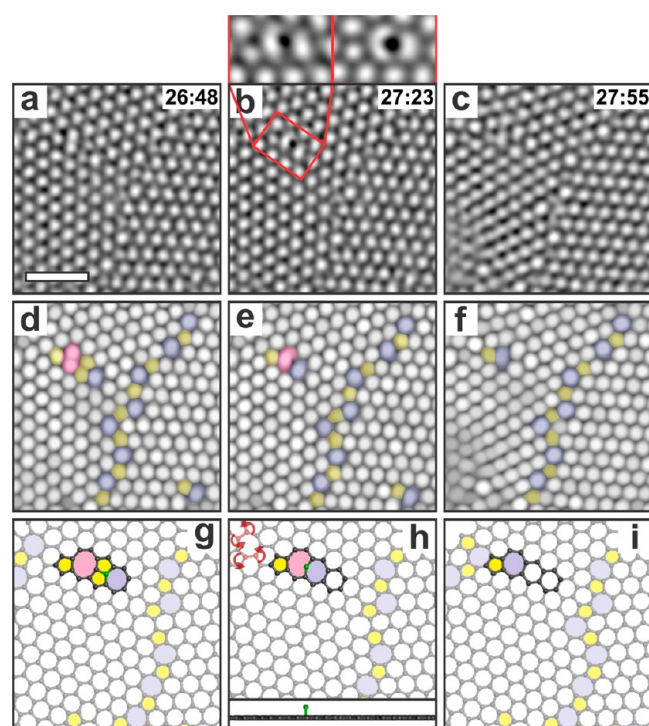


**Figure 11.** Evaporation of a carbon dimer in the GB. (a) FFT reconstructed AC-TEM images of the second-layer graphene at 26 min 48 s. (b) After 35 s, a carbon dimer in the GB is rotated perpendicular to the graphene plane. Magnified view of the flipping dimer is presented on top, along with the multislice simulated TEM image based on the atomic model in (g). (c) The dimer is eventually removed after another 22 s. (d–f) Maximum filtered images of (d–f). (g–i) Corresponding atomic models. The inset in (h) shows its side view. The scale bar in panel a is 1 nm.

suggested by DFT calculation. The energy barriers to further evaporate the vertically stacked dimer are 2.75 and 2.2 eV, respectively. Theoretically the two atoms may also be sputtered one after another, but the energy required for this process is far higher (12.7 eV). [Supporting Information Movie 2](#) shows the dynamic process simulated by high-temperature TBMD.

Here, we discuss why the coalescence of grains is drastically reduced after 11 min. When the grain reaches a certain size, the GBs progressively evolve into a less meandering structure. As a consequence, there is no defect or edge nearby for the GB to interact with. The maximum energy an electron can impart to a carbon atom is  $\sim 19$  eV in our imaging condition (80 kV accelerating voltage, 800 °C), which is not sufficient for a dislocation to make a long distance motion.<sup>56</sup> Although a bond rotation could still be activated at the GB under 80 kV electron irradiation, it is not energetically favorable since the GB has evolved to a relatively straight and symmetric shape (green inset in [Figure 13b](#)). The rotated bond is more likely to quickly restore in another electron collision. In addition, we discover that the stability of GBs is dependent on the misorientation angles. In [Figure 13](#), we presented images of a second-layer graphene taken after 18 min 56 s. Full-time sequential frames are shown in [Figure S4](#). The lattice orientations for the grains 1, 2, and 3 are 0°, 9°, and 38°. The GB between grains 1 and 2 is a low-tilted angle GB made of dislocations pointing to the same direction. The other two with 27° and 38° misorientation angles are high-angle tilt GBs. We observed in total 9 bond rotations and 4 atoms lost in or near the low-angle tilt

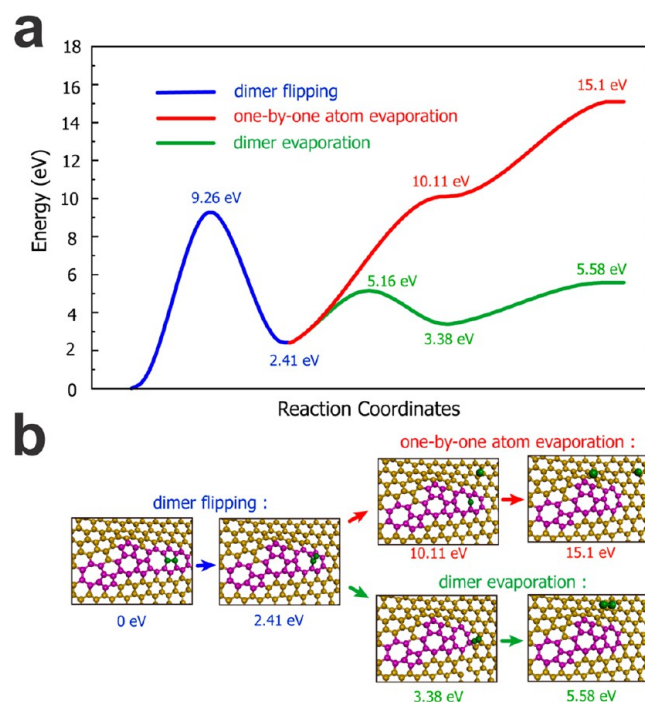


**Figure 12.** DFT calculated energy barriers of two mechanisms for the evaporation of a carbon dimer. (a) Energy curves for the dimer evaporation. In both pathways, the carbon dimer needs to first overcome a 9.26 eV barrier and get vertically stacked (blue curve). The energy barriers to subsequently sputter the dimer as a whole are 2.75 and 2.2 eV, respectively (green curve). The two carbon atoms may also be removed one after another which requires a total energy of 12.69 eV (red curve). (b) Atomic models and DFT calculated relative energies for the moments of dimer evaporation.

boundary between grains 1 and 2 from 18 min 56 s to 27 min 55 s, while 8 bond rotations and only one dimer sputtering (shown in [Figure 10](#)) occurred in the high-angle GB. Considering the lengths of the GBs, it is apparent that the high-angle one possesses higher stability in our imaging condition. This is consistent with the theory proposed by Liu *et al.*<sup>60</sup> As the dislocation density increases with the grain mismatch angle, the strain introduced by the dislocations partially cancels each other, and the out-of-plane distortion caused by the GBs becomes smaller, which has been proven to be robust under electron irradiation.<sup>28</sup> It is worth noting that the top right part of the high-angle GB ([Figure 13a](#)) rotates from the edge to the symmetric line between two grains (gray rectangular in [Figure 13d](#)) in the first 6 min 49 s (migration direction shown in [Figure 13d](#)), which further straightens the GB. Once it was configured into a linear and symmetric shape in [Figure 13b](#), no structural change took place in the next 2 min 10 s. We also see the SW defect (red inset in [Figure 13b](#)) appeared 4 times at the edge of grain 3 during the same period ([Figure S4](#)), which has been experimentally confirmed to help alleviate the strain induced by the high-angle GB in [ref 59](#) and enhance its stability.

## CONCLUSION

We study the *in situ* high-temperature growth of secondary layers of graphene using Au nanoparticles as seeds for heterogeneous nucleation within an AC-TEM. We find that graphene starts to encapsulate the Au nanoparticle at temperatures above 300 °C from carbon material initially

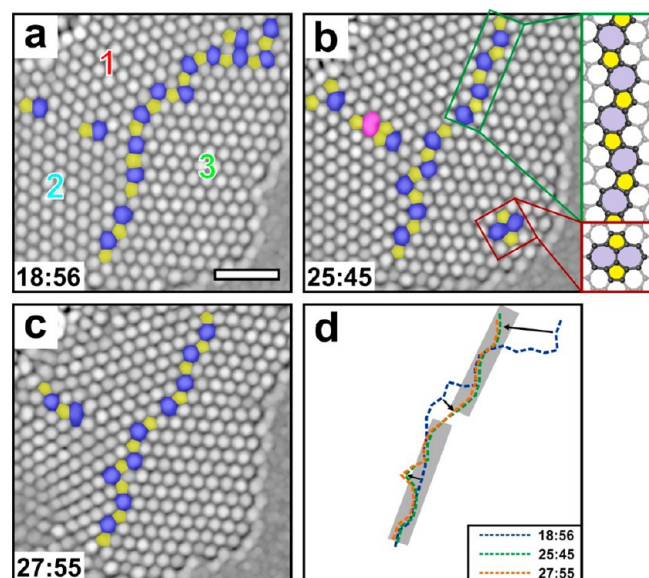


**Figure 13.** The stability of GBs. (a) Maximum filtered TEM images of the second-layer graphene at 18 min 56 s. (b) The same area imaged after 6 min 49 s, with atomic models of the GB between grains 1 and 3, and SW defect near the edge shown in the insets. (c) The same area imaged 2 min 10 s after (b). (d) Dashed lines showing the evolution of the high mismatch angle GB, which are drawn by connecting the central point of adjacent pentagons and heptagons at the boundary. The gray rectangles indicate the symmetric lines between grains. The migration direction of the GB is indicated by black arrows. The scale bar in panel a is 1 nm.

located on the surface of graphene. 600 °C is found to be the optimum temperature to grow a second layer of graphene within our *in situ* environment to study the atomic level dynamics. We kept the TEM chamber pressure at  $\sim 10^{-5}$  Pa to maintain the TEM in a workable condition. Graphene started to grow as carbon molecular precursors arrive at the Au cluster and attach to it. We have also particularly chosen a Au particle on clean and defect-free graphene for the growth experiment, as the contamination coming from the graphene synthesis and transfer process may significantly increase the local hydrocarbon gas pressure and directly lead to the formation of amorphous carbon. The mechanism for growth front propagation is found to be an alternant process of carbon cluster deposition and indentation filling. A detailed study of the edge reveals that the occasionally observed dark contrast lines arise from back-folding of the second layer. Further increasing the temperature to 800 °C slows down growth but accelerates the crystallization of as-grown graphene. The secondary layer starts as highly polycrystalline, but improves its ordering under the combined effect of beam irradiation and increased thermal energy. Large grains grow at the expense of smaller ones *via* multiple bond rotations occurring almost simultaneously. The coalescence of grains near the edge further involves the interaction between GB and edge. The merging of grains stopped when the grain reached a certain size. Afterward the GB migration is dominated by single glide and climb motions of dislocations. This sheds light on how nanoparticle impurities on the surface of graphene could seed multilayer regions during CVD growth of graphene.

## METHODS

**Synthesis of Graphene.** Monolayer graphene was synthesized by atmospheric pressure chemical vapor deposition (CVD) method using a melted copper sheet as the catalytic as previously reported.<sup>10,47</sup> The high-purity copper foil (Alfa Aesar, Puratonic 99.999% pure, 0.1 mm thick) of  $\sim 1$  cm<sup>2</sup> was placed on the molybdenum piece of the same size (Alfa Aesar, 99.95% pure, 0.1 mm thick), and both were loaded into a 1 in. quartz tube in the CVD system. Molybdenum acts as a stable wetting layer to prevent liquid copper from balling. 100 sccm H<sub>2</sub>/Ar (20% H<sub>2</sub> in Ar), 100 sccm CH<sub>4</sub> (1% CH<sub>4</sub> in Ar), and 200 sccm 100% Ar were flowed for 30 min. CH<sub>4</sub> flow was switched off before increasing the hot-zone temperature to 1090 °C. Once the temperature reached 1090 °C, the quartz tube was moved from the room temperature zone to the center of heating zone and annealed for 30 min. The flow of H<sub>2</sub>/Ar was then reduced to 80 sccm, and 10 sccm of 1% CH<sub>4</sub> in Ar was added for 90 min for graphene growth. After growth, the quartz was removed from the heating zone for rapid cooling in the air with the CH<sub>4</sub> off.

**Transfer.** A PMMA scaffold (8 wt % in anisole, 495k molecular weight) was spin-coated onto the graphene sheet at 4700 rpm for 60 s and then baked at 180 °C for 90 s to solidify. Afterward the sample was made up of a molybdenum/copper/graphene/PMMA stack. The copper layer were etched by floating the sample on the mixed solution of iron(III) chloride and hydrochloride, leaving a floating graphene–PMMA film on the top after 48 h. The film was collected using a clean glass slide and transferred onto the surface of the DI water for 30 min, washing away any remaining iron(III) chloride. To further dissolve excess iron chloride, the sample was transferred onto a 10% hydrogen chloride solution for 5 min, before rinsed again in the DI water for 30 min. The film was then transferred onto a SiN TEM grid designed for *in situ* transmission electron microscopy in a heating holder (DENS solutions single tilt 30° fitted with DENS solutions high-temperature EM heater chip with a maximum operating temperature up to 800 °C). The thin SiN membrane on the heating holder contained several windows (size 3 × 0.2 μm) produced using a Zeiss NVision SEM: FIB prior to graphene transfer. These windows were essential to enable HRTEM imaging of the graphene lattice without contrast from the SiN membrane. The grid was then cured at 350 °C for 12 h to burn out PMMA, leaving clean graphene.

**Electron Microscopy.** AC-TEM images were taken at an accelerating voltage of 80 kV, using Oxford's JEOL JEM-2200MCO field emission transmission electron microscope with a CEOS image corrector.<sup>27</sup> Data were recorded using a Gatan Ultrascan 4K × 4K CCD camera with 1–2 s acquisition times and 2 pixel binning. TEM images were processed using ImageJ. Smoothing of images was achieved by using a Gaussian blur filter in ImageJ.

**In Situ Heating Holder.** To perform variable-temperature experiments, we used a commercially available *in situ* heating holder from DENS solutions (SH30-4M-FS). In the DENS solutions holder, heating the sample was achieved by passing a current through a platinum resistive coil imbedded in the TEM chip (DENS solutions DENS-C-30). The resistance of the platinum coil is monitored in a four-point configuration, and the temperature is calculated using the Callendar–Van Dusen equation (with calibration constants provided by the manufacturer).

**DFT Calculation.** The DFT calculations are performed within the generalized gradient approximation of Perdew–Burke–Ernzerhof functional using Vienna *ab initio* simulation package code.<sup>61,62</sup> The basis set contains plane waves up to an energy cutoff of 400 eV. The unit cells are constructed with 200 carbon atoms. The unit cells are periodically repeated in the lateral direction and contain the vacuum region of 30 Å. We choose only one *k* point, the  $\Gamma$  point because the unit cell is enough large. When structural relaxations are performed, the structure is fully relaxed until the force on each atom is smaller than 0.02 eV/Å.

**TBMD Simulation.** The TBMD simulations are performed using a modified environment-dependent tight-binding (EDTB) carbon potential,<sup>63</sup> which is modified from the original EDTB carbon potential to study carbon sp<sup>2</sup> bond networks<sup>64</sup> and has been

successfully applied to investigations of various defect structures in graphene and carbon nanotubes. The details of the TBMD simulation methods have been described in a previous publication.<sup>65</sup> The self-consistent calculations are performed by including a Hubbard-U term in the TB Hamiltonian to describe correctly the charge transfers in carbon atoms of dangling bonds and to prevent the unrealistic overestimation of charge transfers. The equations of motion of the atoms are solved by the fifth-order predictor-corrector algorithm with a time step of 1.0 fs. In the case of TBMD simulation for the merging of two grains *via* three bond rotations shown in Figure 3 and Supporting Information, Movie 1, the simulation unit cell contains 200 atoms. The simulation is started at a temperature of 4000 K under the canonical control of temperature. The temperature is gradually increased to 4800 K under linear temperature control to accelerate the dynamics so that structural reconstruction could be observed during the simulation time. In the case of TBMD simulation for evaporation of a carbon dimer in the GB shown in Figure 7 and Supporting Information, Movie 2, the simulation unit cell contains 200 atoms. The simulation was started at a temperature of 4000 K under the canonical control of temperature and gradually increased to 5000 K. The velocity scaling method was also used to control the temperature.

## ASSOCIATED CONTENT

### Supporting Information

The Supporting Information is available free of charge on the ACS Publications website at DOI: 10.1021/acsnano.6b04356.

High-temperature TBMD simulations; merging of two grains *via* three bond rotations (AVI)

Dynamic process simulated by high-temperature TBMD; evaporation of a carbon dimer in the GB (AVI)

TEM images showing the growth of second-layer graphene at 600 °C; EDX characterization of nanocrystals; TEM images showing another example of grain coalescence; full sequencing TEM frames from 18 min 56 s to 27 min 55 s (PDF)

## AUTHOR INFORMATION

### Corresponding Authors

\*E-mail: [Jamie.warner@materials.ox.ac.uk](mailto:Jamie.warner@materials.ox.ac.uk).

\*E-mail: [gdllee@snu.ac.kr](mailto:gdllee@snu.ac.kr).

### Author Contributions

<sup>||</sup>These authors contributed equally.

### Notes

The authors declare no competing financial interest.

## ACKNOWLEDGMENTS

J.H.W. thanks the support from the Royal Society. C.G. thanks the support from the Clarendon Fund. G.-D.L. acknowledges support from the Supercomputing Center/Korea Institute of Science and Technology Information with supercomputing resources (KSC-2015-C3-011) and from NRF grant (RIAM no. 2010-0012670). S.H. thanks the support from Nano Material Technology Development Program (2012M3A7B4049888) through NRF-MSIP and Priority Research Center Program (2010-0020207) through NRF-MOE.

## REFERENCES

- (1) Li, X.; Cai, W.; An, J.; Kim, S.; Nah, J.; Yang, D.; Piner, R.; Velamakanni, A.; Jung, I.; Tutuc, E.; Banerjee, S. K.; Colombo, L.; Ruoff, R. S. Large-Area Synthesis of High-Quality and Uniform Graphene Films on Copper Foils. *Science* **2009**, *324*, 1312–1314.
- (2) Alemán, B.; Regan, W.; Aloni, S.; Altoe, V.; Alem, N.; Girit, C.; Geng, B.; Maserati, L.; Crommie, M.; Wang, F.; Zettl, A. Transfer-Free

Batch Fabrication of Large-Area Suspended Graphene Membranes. *ACS Nano* **2010**, *4*, 4762–4768.

- (3) Bhaviripudi, S.; Jia, X.; Dresselhaus, M. S.; Kong, J. Role of Kinetic Factors in Chemical Vapor Deposition Synthesis of Uniform Large Area Graphene Using Copper Catalyst. *Nano Lett.* **2010**, *10*, 4128–4133.

- (4) Bae, S.; Kim, H.; Lee, Y.; Xu, X.; Park, J.-S.; Zheng, Y.; Balakrishnan, J.; Lei, T.; Kim, H. R.; Song, Y. I.; Kim, Y.-J.; Kim, K. S.; Ozyilmaz, B.; Ahn, J.-H.; Hong, B. H.; Iijima, S. Roll-to-Roll Production of 30-Inch Graphene Films for Transparent Electrodes. *Nat. Nanotechnol.* **2010**, *5*, 574–578.

- (5) Li, X.; Magnuson, C. W.; Venugopal, A.; Tromp, R. M.; Hannon, J. B.; Vogel, E. M.; Colombo, L.; Ruoff, R. S. Large-Area Graphene Single Crystals Grown by Low-Pressure Chemical Vapor Deposition of Methane on Copper. *J. Am. Chem. Soc.* **2011**, *133*, 2816–2819.

- (6) Mattevi, C.; Kim, H.; Chhowalla, M. A Review of Chemical Vapour Deposition of Graphene on Copper. *J. Mater. Chem.* **2011**, *21*, 3324–3334.

- (7) Kim, H.; Mattevi, C.; Calvo, M. R.; Oberg, J. C.; Artiglia, L.; Agnoli, S.; Hirjibehedin, C. F.; Chhowalla, M.; Saiz, E. Activation Energy Paths for Graphene Nucleation and Growth on Cu. *ACS Nano* **2012**, *6*, 3614–3623.

- (8) Yu, Q.; Jauregui, L. A.; Wu, W.; Colby, R.; Tian, J.; Su, Z.; Cao, H.; Liu, Z.; Pandey, D.; Wei, D.; Chung, T. F.; Peng, P.; Guisinger, N. P.; Stach, E. A.; Bao, J.; Pei, S.-S.; Chen, Y. P. Control and Characterization of Individual Grains and Grain Boundaries in Graphene Grown by Chemical Vapour Deposition. *Nat. Mater.* **2011**, *10*, 443–449.

- (9) Wu, W.; Jauregui, L. A.; Su, Z.; Liu, Z.; Bao, J.; Chen, Y. P.; Yu, Q. Growth of Single Crystal Graphene Arrays by Locally Controlling Nucleation on Polycrystalline Cu Using Chemical Vapor Deposition. *Adv. Mater.* **2011**, *23*, 4898–4903.

- (10) Wu, Y. A.; Fan, Y.; Speller, S.; Creeth, G. L.; Sadowski, J. T.; He, K.; Robertson, A. W.; Allen, C. S.; Warner, J. H. Large Single Crystals of Graphene on Melted Copper Using Chemical Vapor Deposition. *ACS Nano* **2012**, *6*, 5010–5017.

- (11) Hao, Y.; Bharathi, M. S.; Wang, L.; Liu, Y.; Chen, H.; Nie, S.; Wang, X.; Chou, H.; Tan, C.; Fallahzad, B.; Ramanarayan, H.; Magnuson, C. W.; Tutuc, E.; Jakobson, B. I.; McCarty, K. F.; Zhang, Y.-W.; Kim, P.; Hone, J.; Colombo, L.; Ruoff, R. S. The Role of Surface Oxygen in the Growth of Large Single-Crystal Graphene on Copper. *Science* **2013**, *342*, 720–723.

- (12) Geng, D.; Meng, L.; Chen, B.; Gao, E.; Yan, W.; Yan, H.; Luo, B.; Xu, J.; Wang, H.; Mao, Z.; Xu, Z.; He, L.; Zhang, Z.; Peng, L.; Yu, G. Controlled Growth of Single-Crystal Twelve-Pointed Graphene Grains on a Liquid Cu Surface. *Adv. Mater.* **2014**, *26*, 6423–6429.

- (13) Grantab, R.; Shenoy, V. B.; Ruoff, R. S. Anomalous Strength Characteristics of Tilt Grain Boundaries in Graphene. *Science* **2010**, *330*, 946–948.

- (14) Wei, Y.; Wu, J.; Yin, H.; Shi, X.; Yang, R.; Dresselhaus, M. The Nature of Strength Enhancement and Weakening by Pentagon–heptagon Defects in Graphene. *Nat. Mater.* **2012**, *11*, 759–763.

- (15) Kotakoski, J.; Meyer, J. C. Mechanical Properties of Polycrystalline Graphene Based on a Realistic Atomistic Model. *Phys. Rev. B: Condens. Matter Phys.* **2012**, *85*, 195447.

- (16) Rasool, H. I.; Ophus, C.; Zhang, Z.; Crommie, M. F.; Jakobson, B. I.; Zettl, A. Conserved Atomic Bonding Sequences and Strain Organization of Graphene Grain Boundaries. *Nano Lett.* **2014**, *14*, 7057–7063.

- (17) Rasool, H. I.; Ophus, C.; Klug, W. S.; Zettl, A.; Gimzewski, J. K. Measurement of the Intrinsic Strength of Crystalline and Polycrystalline Graphene. *Nat. Commun.* **2013**, *4*, 2811.

- (18) Lee, G.-H.; Cooper, R. C.; An, S. J.; Lee, S.; van der Zande, A.; Petrone, N.; Hammerberg, A. G.; Lee, C.; Crawford, B.; Oliver, W.; Kysar, J. W.; Hone, J. High-Strength Chemical-Vapor-Deposited Graphene and Grain Boundaries. *Science* **2013**, *340*, 1073–1076.

- (19) Yazyev, O. V.; Louie, S. G. Electronic Transport in Polycrystalline Graphene. *Nat. Mater.* **2010**, *9*, 806–809.

- (20) Tsen, A. W.; Brown, L.; Levendorf, M. P.; Ghahari, F.; Huang, P. Y.; Havener, R. W.; Ruiz-Vargas, C. S.; Muller, D. A.; Kim, P.; Park, J. Tailoring Electrical Transport across Grain Boundaries in Polycrystalline Graphene. *Science* **2012**, *336*, 1143–1146.
- (21) Yasaei, P.; Kumar, B.; Hantehzadeh, R.; Kayyalha, M.; Baskin, A.; Reppin, N.; Wang, C.; Klie, R. F.; Chen, Y. P.; Král, P.; Salehi-Khojin, A. Chemical Sensing with Switchable Transport Channels in Graphene Grain Boundaries. *Nat. Commun.* **2014**, *5*, 4911.
- (22) Hashimoto, A.; Suenaga, K.; Gloter, A.; Urita, K.; Iijima, S. Direct Evidence for Atomic Defects in Graphene Layers. *Nature* **2004**, *430*, 870–873.
- (23) Jeong, B.; Ihm, J.; Lee, G.-D. Stability of Dislocation Defect with Two Pentagon-Heptagon Pairs in Graphene. *Phys. Rev. B: Condens. Matter Mater. Phys.* **2008**, *78*, 165403.
- (24) Yazyev, O. V.; Louie, S. G. Topological Defects in Graphene: Dislocations and Grain Boundaries. *Phys. Rev. B: Condens. Matter Mater. Phys.* **2010**, *81*, 195420.
- (25) Carlsson, J. M.; Ghiringhelli, L. M.; Fasolino, A. Theory and Hierarchical Calculations of the Structure and Energetics of [0001] Tilt Grain Boundaries in Graphene. *Phys. Rev. B: Condens. Matter Mater. Phys.* **2011**, *84*, 165423.
- (26) Kim, K.; Lee, Z.; Regan, W.; Kisielowski, C.; Crommie, M. F.; Zettl, A. Grain Boundary Mapping in Polycrystalline Graphene. *ACS Nano* **2011**, *5*, 2142–2146.
- (27) Warner, J. H.; Margine, E. R.; Mukai, M.; Robertson, A. W.; Giustino, F.; Kirkland, A. I. Dislocation-Driven Deformations in Graphene. *Science* **2012**, *337*, 209–212.
- (28) Lehtinen, O.; Kurasch, S.; Krashennnikov, A. V.; Kaiser, U. Atomic Scale Study of the Life Cycle of a Dislocation in Graphene from Birth to Annihilation. *Nat. Commun.* **2013**, *4*, 2098.
- (29) Lee, G.-D.; Yoon, E.; Hwang, N.-M.; Wang, C.-Z.; Ho, K.-M. Formation and Development of Dislocation in Graphene. *Appl. Phys. Lett.* **2013**, *102*, 021603.
- (30) Lee, G.-D.; Yoon, E.; Wang, C.-Z.; Ho, K.-M. Atomistic Processes of Grain Boundary Motion and Annihilation in Graphene. *J. Phys.: Condens. Matter* **2013**, *25*, 155301.
- (31) Warner, J. H.; Fan, Y.; Robertson, A. W.; He, K.; Yoon, E.; Lee, G.-D. Rippling Graphene at the Nanoscale through Dislocation Addition. *Nano Lett.* **2013**, *13*, 4937–4944.
- (32) Zhang, Z.; Yang, Y.; Xu, F.; Wang, L.; Yakobson, B. I. Unraveling the Sinuous Grain Boundaries in Graphene. *Adv. Funct. Mater.* **2015**, *25*, 367–373.
- (33) Albrecht, T. R.; Mizes, H. A.; Nogami, J.; Park, S.; Quate, C. F. Observation of Tilt Boundaries in Graphite by Scanning Tunneling Microscopy and Associated Multiple Tip Effects. *Appl. Phys. Lett.* **1988**, *52*, 362–364.
- (34) Huang, P. Y.; Ruiz-Vargas, C. S.; van der Zande, A. M.; Whitney, W. S.; Levendorf, M. P.; Kevek, J. W.; Garg, S.; Alden, J. S.; Hustedt, C. J.; Zhu, Y.; Park, J.; McEuen, P. L.; Muller, D. A. Grains and Grain Boundaries in Single-Layer Graphene Atomic Patchwork Quilts. *Nature* **2011**, *469*, 389–392.
- (35) An, J.; Voelkl, E.; Suk, J. W.; Li, X.; Magnuson, C. W.; Fu, L.; Tiemeijer, P.; Bischoff, M.; Freitag, B.; Popova, E.; Ruoff, R. S. Domain (Grain) Boundaries and Evidence of “Twinlike” Structures in Chemically Vapor Deposited Grown Graphene. *ACS Nano* **2011**, *5*, 2433–2439.
- (36) Kurasch, S.; Kotakoski, J.; Lehtinen, O.; Skákalová, V.; Smet, J.; Krill, C. E.; Krashennnikov, A. V.; Kaiser, U. Atom-by-Atom Observation of Grain Boundary Migration in Graphene. *Nano Lett.* **2012**, *12*, 3168–3173.
- (37) Yang, B.; Xu, H.; Lu, J.; Loh, K. P. Periodic Grain Boundaries Formed by Thermal Reconstruction of Polycrystalline Graphene Film. *J. Am. Chem. Soc.* **2014**, *136*, 12041–12046.
- (38) Lahiri, J.; Lin, Y.; Bozkurt, P.; Oleynik, I. I.; Batzill, M. An Extended Defect in Graphene as a Metallic Wire. *Nat. Nanotechnol.* **2010**, *5*, 326–329.
- (39) Kim, D.; Kim, Y.; Ihm, J.; Yoon, E.; Lee, G.-D. Atomic-Scale Mechanism of Grain Boundary Motion in Graphene. *Carbon* **2015**, *84*, 146–150.
- (40) Westenfelder, B.; Meyer, J. C.; Biskupek, J.; Kurasch, S.; Scholz, F.; Krill, C. E.; Kaiser, U. Transformations of Carbon Adsorbates on Graphene Substrates under Extreme Heat. *Nano Lett.* **2011**, *11*, 5123–5127.
- (41) Liu, Z.; Lin, Y.-C.; Lu, C.-C.; Yeh, C.-H.; Chiu, P.-W.; Iijima, S.; Suenaga, K. *In Situ* Observation of Step-Edge in-Plane Growth of Graphene in a STEM. *Nat. Commun.* **2014**, *5*, 4055.
- (42) Dong, G. C.; van Baarle, D. W.; Rost, M. J.; Frenken, J. W. M. Graphene Formation on Metal Surfaces Investigated by *In-Situ* Scanning Tunneling Microscopy. *New J. Phys.* **2012**, *14*, 53033.
- (43) Günther, S.; Dänhardt, S.; Ehrensperger, M.; Zeller, P.; Schmitt, S.; Wintterlin, J. High-Temperature Scanning Tunneling Microscopy Study of the Ordering Transition of an Amorphous Carbon Layer into Graphene on Ruthenium(0001). *ACS Nano* **2013**, *7*, 154–164.
- (44) Patera, L. L.; Africh, C.; Weatherup, R. S.; Blume, R.; Bhardwaj, S.; Castellarin-Cudia, C.; Knop-Gericke, A.; Schloegl, R.; Comelli, G.; Hofmann, S.; Cepek, C. *In Situ* Observations of the Atomistic Mechanisms of Ni Catalyzed Low Temperature Graphene Growth. *ACS Nano* **2013**, *7*, 7901–7912.
- (45) Dong, G.; Frenken, J. W. M. Kinetics of Graphene Formation on Rh(111) Investigated by *In Situ* Scanning Tunneling Microscopy. *ACS Nano* **2013**, *7*, 7028–7033.
- (46) Günther, S.; Dänhardt, S.; Wang, B.; Bocquet, M.-L.; Schmitt, S.; Wintterlin, J. Single Terrace Growth of Graphene on a Metal Surface. *Nano Lett.* **2011**, *11*, 1895–1900.
- (47) Fan, Y.; He, K.; Tan, H.; Speller, S.; Warner, J. H. Crack-Free Growth and Transfer of Continuous Monolayer Graphene Grown on Melted Copper. *Chem. Mater.* **2014**, *26*, 4984–4991.
- (48) He, K.; Robertson, A. W.; Fan, Y.; Allen, C. S.; Lin, Y.-C.; Suenaga, K.; Kirkland, A. I.; Warner, J. H. Temperature Dependence of the Reconstruction of Zigzag Edges in Graphene. *ACS Nano* **2015**, *9*, 4786–4795.
- (49) Warner, J. H.; Lin, Y.-C.; He, K.; Koshino, M.; Suenaga, K. Stability and Spectroscopy of Single Nitrogen Dopants in Graphene at Elevated Temperatures. *ACS Nano* **2014**, *8*, 11806–11815.
- (50) Sutter, E.; Sutter, P.; Zhu, Y. Assembly and Interaction of Au/C Core-Shell Nanostructures: *In Situ* Observation in the Transmission Electron Microscope. *Nano Lett.* **2005**, *5*, 2092–2096.
- (51) Koga, K.; Ikeshoji, T.; Sugawara, K. Size- and Temperature-Dependent Structural Transitions in Gold Nanoparticles. *Phys. Rev. Lett.* **2004**, *92*, 115507.
- (52) Shu, H.; Chen, X.; Tao, X.; Ding, F. Edge Structural Stability and Kinetics of Graphene Chemical Vapor Deposition Growth. *ACS Nano* **2012**, *6*, 3243–3250.
- (53) Koskinen, P.; Malola, S.; Häkkinen, H. Self-Passivating Edge Reconstructions of Graphene. *Phys. Rev. Lett.* **2008**, *101*, 115502.
- (54) Liu, Z.; Suenaga, K.; Harris, P. J. F.; Iijima, S. Open and Closed Edges of Graphene Layers. *Phys. Rev. Lett.* **2009**, *102*, 015501.
- (55) Meyer, J. C.; Geim, A. K.; Katsnelson, M. I.; Novoselov, K. S.; Booth, T. J.; Roth, S. The Structure of Suspended Graphene Sheets. *Nature* **2007**, *446*, 60–63.
- (56) Gong, C.; Robertson, A. W.; He, K.; Lee, G.-D.; Yoon, E.; Allen, C. S.; Kirkland, A. I.; Warner, J. H. Thermally Induced Dynamics of Dislocations in Graphene at Atomic Resolution. *ACS Nano* **2015**, *9*, 10066–10075.
- (57) Li, L.; Reich, S.; Robertson, J. Defect Energies of Graphite: Density-Functional Calculations. *Phys. Rev. B: Condens. Matter Mater. Phys.* **2005**, *72*, 184109.
- (58) Kim, Y.; Ihm, J.; Yoon, E.; Lee, G.-D. Dynamics and Stability of Divacancy Defects in Graphene. *Phys. Rev. B: Condens. Matter Mater. Phys.* **2011**, *84*, 075445.
- (59) Gong, C.; He, K.; Robertson, A. W.; Yoon, E.; Lee, G.-D.; Warner, J. H. Spatially Dependent Lattice Deformations for Dislocations at the Edges of Graphene. *ACS Nano* **2015**, *9*, 656–662.
- (60) Liu, T. H.; Gajewski, G.; Pao, C. W.; Chang, C. C. Structure, Energy, and Structural Transformations of Graphene Grain Boundaries from Atomistic Simulations. *Carbon* **2011**, *49*, 2306–2317.
- (61) Perdew, J.; Burke, K.; Ernzerhof, M. Generalized Gradient Approximation Made Simple. *Phys. Rev. Lett.* **1996**, *77*, 3865–3868.

(62) Kresse, G.; Furthmüller, J. Efficient Iterative Schemes for *Ab Initio* Total-Energy Calculations Using a Plane-Wave Basis Set. *Phys. Rev. B: Condens. Matter Mater. Phys.* **1996**, *54*, 11169–11186.

(63) Lee, G. Do; Wang, C. Z.; Yoon, E.; Hwang, N. M.; Ho, K. M. Vacancy Defects and the Formation of Local Haeckelite Structures in Graphene from Tight-Binding Molecular Dynamics. *Phys. Rev. B: Condens. Matter Mater. Phys.* **2006**, *74*, 245411.

(64) Lee, G.-D.; Wang, C. Z.; Yoon, E.; Hwang, N.-M.; Kim, D.-Y.; Ho, K. M. Diffusion, Coalescence, and Reconstruction of Vacancy Defects in Graphene Layers. *Phys. Rev. Lett.* **2005**, *95*, 205501.

(65) Tang, M. S.; Wang, C. Z.; Chan, C. T.; Ho, K. M. Environment-Dependent Tight-Binding Potential Model. *Phys. Rev. B: Condens. Matter Mater. Phys.* **1996**, *53*, 979–982.